PCCP

Accepted Manuscript

ROYAL SOCIETY OF CHEMISTRY

www.rsc.org/pccp

Journal Name

RSCPublishing

ARTICLE

Large impact of reorganization energy on photovoltaic conversion due to interfacial charge-transfer transitions

Jun-ichi Fujisawa[ab]

Cite this: DOI: 10.1039/x0xx00000x

Received 00th January 2012,
Accepted 00th January 2012

DOI: 10.1039/x0xx00000x

www.rsc.org/

Interfacial charge-transfer (ICT) transitions are expected to be a novel charge-separation mechanism for efficient photovoltaic conversion featuring one-step charge separation without energy loss. Photovoltaic conversion due to ICT transitions has been investigated using several TiO_2-organic hybrid materials that show organic-to-inorganic ICT transitions in the visible region. In applications of ICT transitions to photovoltaic conversion, there is a significant problem that rapid carrier recombination is caused by organic-inorganic electronic coupling that is necessary for the ICT transitions. In order to solve this problem, in this work, I have theoretically studied light-to-current conversions due to the ICT transitions on the basis of the Marcus theory with density functional theory (DFT) and time-dependent DFT (TD-DFT) calculations. An apparent correlation between the reported incident photon-to-current conversion efficiencies (IPCE) and calculated reorganization energies was clearly found, in which the IPCE increases with decreasing the reorganization energy consistent with the Marcus theory in the inverted region. This activation-energy dependence was systematically explained by the equation formulated by the Marcus theory based on a simple excited-state kinetic scheme. This result indicates that the reduction of the reorganization energy can suppress the carrier recombination and enhance the IPCE. The reorganization energy is predominantly governed by the structural change in the chemical-adsorption moiety between the ground and ICT excited states. This work provides crucial knowledge for efficient photovoltaic conversion due to ICT transitions.

Introduction

Photovoltaic conversion devices including solar cells consist of electron-donating (*p*-type semiconductors) and electron-accepting materials (*n*-type semiconductors), as shown in Fig. 1. In them, photovoltaic conversion occurs via (i) light absorption due to internal electronic transitions such as inter-band electronic transitions in inorganic semiconductors or intra-molecular electronic transitions in dyes and (ii) subsequent interfacial charge-separation of photogenerated electrons and holes. The latter interfacial charge-separation occurs with energy loss of at least ca. 0.2-0.3 eV. In order to eliminate this energy loss, interfacial charge-transfer (ICT) transitions should be employed, because ICT transitions in principle directly induce charge separation without energy loss. (Fig. 1) Photovoltaic conversion by ICT transitions have been studied from 2000 by employing hybrid materials formed from TiO_2 nanoparticles and enediol compounds (ascorbic acid

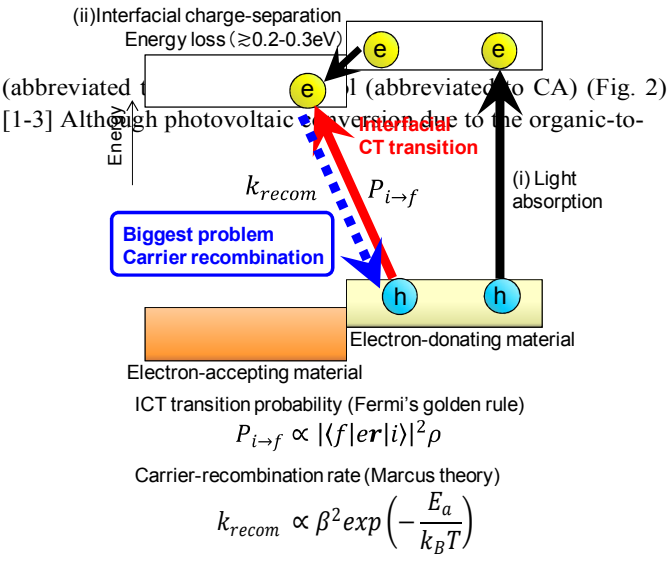

(abbreviated t l (abbreviated to CA) (Fig. 2) [1-3] Although photovoltaic conversion due to the organic-to-

Fig. 1. Schematic picture of fundamental structure of solar cells, photovoltaic conversion processes, and ICT transitions featuring one-step charge separation together with the equations of ICT transition probability and carrier-recombination rate.

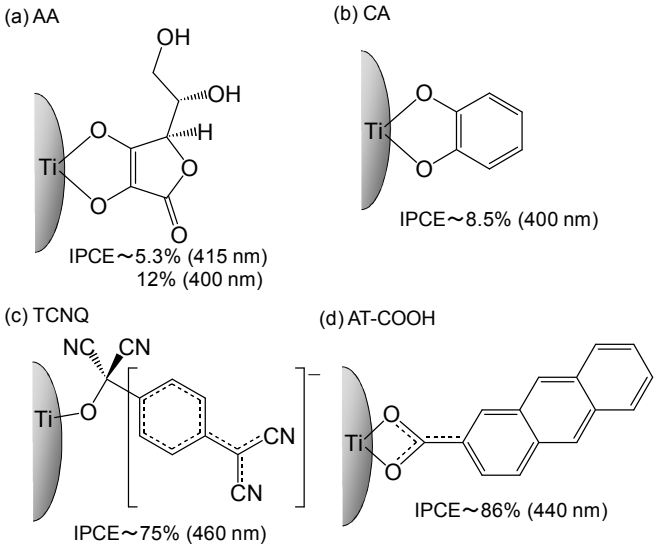

Fig. 2. TiO_2 nanoparticles chemically adsorbed with organic molecules showing ICT absorption and reported IPCE maximum values.

inorganic ICT transitions was first demonstrated with those materials, the observed incident photon-to-current conversion efficiencies (IPCE) were reported to be less than about 10%, as shown in Figs. 2(a) and 2(b).[1-3] In addition, Wang *et al*. have demonstrated that carrier recombination occurs quite rapidly within ca. 2 psec, which results in the low IPCE values. Therefore, suppression of the rapid carrier recombination is the most significant problem for applications of ICT transitions to photovoltaic conversion. However, very little effort has been devoted to this problem, since it was considered that such a rapid carrier recombination would be the intrinsic property for ICT transitions. This is because electronic coupling at organic-inorganic interfaces not only enhances the transition dipole moment ($\langle f|\boldsymbol{er}|i\rangle$) of ICT transitions, but also increases the transfer integral (β) of carrier recombination, as shown in Fig. 1.

On the other hand, it was reported in 2005 that the lead-iodide nanowire perovskite ($MVPb_2I_6$) with organic electron-acceptor methylviologen (MV^{2+}) generates photocurrent due to the ICT transitions under applied voltage much more efficiently than the intra-wire electronic transitions. This result reveals the high potential of ICT transitions in applications to photovoltaic conversion. In addition, the quite long lifetime ($\gtrsim$ 1 msec) of photogenerated carriers in $MVPb_2I_6$ was confirmed by the steady-state photoinduced absorption measurement. This result indicates that the above mentioned rapid carrier recombination is not an intrinsic property of ICT transitions and can be suppressed.

Recently, efficient light-to-current conversions due to ICT transitions were first demonstrated employing the two TiO_2-organic hybrid materials. One is the surface complex formed from TiO_2 nanoparticles and 7,7,8,8-tetracyanoquinodimethane (abbreviated to TCNQ) showing IPCE of ca. 75% (without applied voltage)[9], as shown in Fig. 2(c). The other is TiO_2 nanoparticles chemically adsorbed with

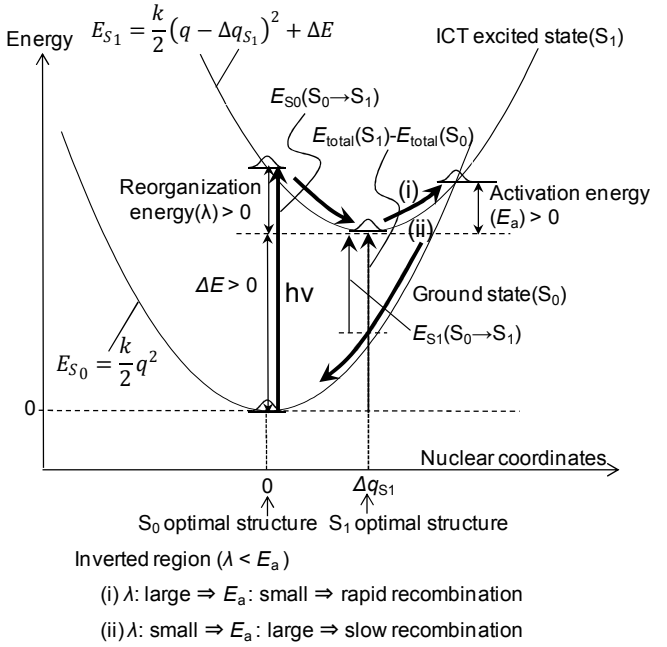

Fig. 3. Schematic diagram of potential curves of the S_0 and S_1 states in the Marcus's inverted region.

2-anthroic acid (abbreviated to AT-COOH) showing IPCE of exceeding 85% (without applied voltage), as shown in Fig. 2(d)[10]. In these hybrids, carrier recombination is considered to be suppressed effectively. However, the questions of why carrier recombination is suppressed in TiO_2-TCNQ and TiO_2-OOC-AT and what is the key factor for it still remain to be resolved. To answer these questions, in this work, I have theoretically studied photovoltaic conversion and carrier recombination in all the reported ICT-transition systems (Fig. 2) on the basis of the Marcus theory [11,12] with density functional theory (DFT) and time-dependent DFT (TD-DFT) calculations.

Fig. 3 shows quadratic harmonic potential curves with the same curvature for the ground singlet (S_0) state and lowest-energy ICT excited singlet (S_1) states. In the Marcus theory, carrier recombination occurs via thermal excitation of the S_1 state and subsequent jumping to the S_0 potential curve at the cross point. Thus, the activation energy ($E_a > 0$) in Fig. 3 is a key factor to control the carrier-recombination rate (k_{recom}), as shown by the following equation [11,12].

$$k_{recom} = \frac{2\pi^2}{h}\frac{\beta^2}{\sqrt{\pi\lambda k_B T}} exp\left(-\frac{E_a}{k_B T}\right) \quad (1)$$

h, k_B, T, and β are the Plank constant, Boltzmann constant, and absolute temperature, the transfer integral between the S_0 and S_1 states at the cross point, respectively. The activation energy is expressed by the following equation.

$$E_a = \frac{(\lambda - \Delta E)^2}{4\lambda} \quad (2)$$

λ and ΔE are a reorganization energy ($\lambda > 0$) and a free-energy difference ($\Delta E > 0$) between the S_0 and S_1 optimal states, respectively, as shown in Fig. 3. TiO_2-CA in Fig. 2 was reported to exist in the Marcus's inverted region ($\lambda < \Delta E$) in Fig. 3.[8] In the inverted region, the activation energy increases with the decrease of the reorganization energy and decreases with the increase of the reorganization energy (Fig. 3). Therefore, if the reorganization energy can be reduced, the carrier recombination can be suppressed according to the Marcus theory.

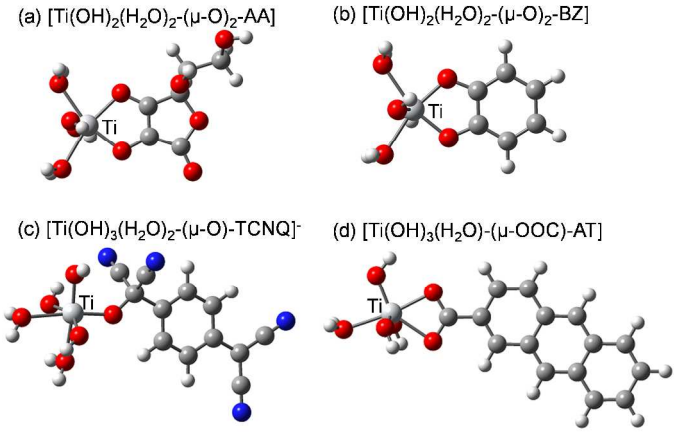

Fig. 4. Optimized structures in the S_0 states of (a) $[Ti(OH)_2(H_2O)_2$-(μ-O)$_2$-AA], (b) $[Ti(OH)_2(H_2O)_2$-(μ-O)$_2$-BZ], (c) $[Ti(OH)_3(H_2O)_2$-(μ-O)-TCNQ]$^-$ and (d) $[Ti(OH)_3(H_2O)$-(μ-OOC)-AT]. Gray: carbon, white: hydrogen, blue: nitrogen, red: oxygen, large white: titanium atom.

Computational details

In the DFT and TD-DFT calculations, at first, four model compounds of $[Ti(OH)_2(H_2O)_2$-(μ-O)$_2$-AA], $[Ti(OH)_2(H_2O)_2$-(μ-O)$_2$-BZ] (BZ: benzene), $[Ti(OH)_3(H_2O)_2$-(μ-O)-TCNQ]$^-$, and $[Ti(OH)_3(H_2O)$-(μ-OOC)-AT] (AT: anthracene) were examined by simplifying a TiO_2 nanoparticle in Fig. 2 with a mono-nuclear Ti complex, as shown in Fig. 4. The respective adsorption structures were reported in the literature [1-3,9,10,13-15]. Such mono-Ti model complexes have been widely used for the calculations of ICT transitions in TiO_2 nanoparticle adsorbed with the organic molecules, well reproducing the energies of the ICT absorption bands.[3,10,14]

The structures, energies and electronic distributions of molecular orbitals, and total energies (abbreviated to $E_{total}(S_0)$) in the S_0 optimized structures of the four model compounds were calculated by DFT [16] with the B3LYP functional [17,18] and 6-31G+(d,p) basis set [19,20]. The B3LYP functional has been widely employed for the calculation of ICT transitions, well reproducing the charge-transfer properties. [10,13] The structures, energies and electronic distributions of molecular orbitals, and total energies (abbreviated to $E_{total}(S_1)$) in the S_1 optimized structures of the four model compounds were calculated by TD-DFT [21] at the same level of theory, using the S_0 optimized structures as initial structures. Since the mono-Ti model complexes are not suitable to estimate the reorganization energy in TiO_2 nanoparticles (average size: ca. 15-20 nm) used in the experiments, in the TD-DFT calculations the coordinates of all the OH^- and H_2O ligands were kept frozen to those of the S_0 optimal structures. Thus, calculated reorganization energies in this work are attributed to structural reorganizations in the organic and chemical adsorption moieties. The lowest singlet vertical electronic-excitation energies (abbreviated to $E_{S0}(S_0 \rightarrow S_1)$ and $E_{S1}(S_0 \rightarrow S_1)$, respectively) in the S_0 and S_1 optimized structures of the model compounds were calculated by TD-DFT. Reorganization energies are estimated by the following equation (Fig. 3).

$$\lambda = E_{S_0}(S_0 \rightarrow S_1) - \left(E_{total}(S_1) - E_{total}(S_0)\right) \quad (3)$$

Reorganization energies estimated by this equation were confirmed to be in good agreement with those estimated from the difference (2λ) between ($E_{S0}(S_0 \rightarrow S_1)$ and $E_{S1}(S_0 \rightarrow S_1)$). In all the calculations, solvation effects of acetonitrile used in the reported experiments [3,9,10] were taken into account with the conductor-like polarizable continuum model (CPCM) [22,23], since CPCM is one of successful solvation models. [24] All the calculations were performed by using a Gaussian 09 software [25].

In order to examine the functional dependence of reorganization energies, DFT and TD-DFT calculations were also performed by employing the CAM-B3LYP functional [26] that was reported to more quantitatively reproduce charge-transfer excitation energies. [27] CAM-B3LYP provided very close reorganization energies to those calculated by using B3LYP, as described in the supporting information.

Results and discussion

Structures and ICT transitions in S_0 optimized structures

At first, ICT transitions in the S_0 optimized structures of the four model compounds were examined. Fig. 5 shows the calculated electronic-excitation spectra in the S_0 optimized structures (Fig. 4) of the model compounds. $[Ti(OH)_2(H_2O)_2$-(μ-O)$_2$-AA] shows two ICT electronic excitations at 566 and 468 nm due to electronic transitions from the highest occupied molecular orbital (HOMO) to the lowest unoccupied molecular orbital (LUMO) and the second lowest unoccupied molecular orbital (LUMO+1), respectively. The dominant ICT excitation at 468 nm corresponds to the reported IPCE maximum at 400 or 415 nm (Fig. 2(a)) in TiO_2-AA.[1,2] Similarly, $[Ti(OH)_2(H_2O)_2$-(μ-O)$_2$-BZ] exhibits two ICT absorption bands at 514 and 435 nm due to the HOMO→LUMO and HOMO→LUMO+1 transitions, respectively. The strong HOMO→LUMO+1 band at 435 nm corresponds to the IPCE maximum at 400 nm (Fig. 2(b)) in TiO_2-CA.[3] For $[Ti(OH)_3(H_2O)_2$-(μ-O)-TCNQ]$^-$, three ICT excitations occur at 514, 445, and 432 nm, which are attributed to electronic transitions from the HOMO to LUMO, LUMO+1, and the second lowest unoccupied molecular orbital (LUMO+2). The two dominant peaks at 445 and 432 nm correspond to the IPCE maximum at 460 nm (Fig. 2(c)) in TiO_2-TCNQ. [9,13-15]

$[Ti(OH)_3(H_2O)$-(μ-OOC)-AT] shows an ICT excitation due to the HOMO→LUMO transition at 430 nm, which is close to the wavelength (440 nm) of the IPCE maximum at 440 nm (Fig. 2(c)) in TiO_2-OOC-AT.[10] Therefore, all the model compounds show ICT bands in the visible region consistent with the experimental results.[1-3,9,10,13-15] The dominant ICT excitations in the former three compounds are assigned to the higher ICT excitations. Since it is well-known that non-radiative relaxations from higher-energy electronically-excited states to the S_1 state take place quite quickly within a few picoseconds according to the energy-gap law, the reported IPCE maximum values in Fig. 2 are associated with carrier recombination from the S_1 to S_0 state. The calculated $E_{total}(S_0)$, $E_{S0}(S_0 \rightarrow S_1)$ and $S_0 \rightarrow S_1$ excited-state wavefunctions are summarized in Table 1.

Table 1. Calculated total energies ($E_{total}(S_0)$ and $E_{total}(S_1)$) in the S_0 and S_1optimized structures of $[Ti(OH)_2(H_2O)_2$-(μ-O)$_2$-AA], $[Ti(OH)_2(H_2O)_2$-(μ-O)$_2$-CA], $[Ti(OH)_3(H_2O)_2$-(μ-O)-TCNQ]$^-$, and $[Ti(OH)_3(H_2O)$-(μ-OOC)-AT] and calculated lowest excitation energies ($E_{S0}(S_0 \rightarrow S_1)$) and excited-state wavefunctions in the S_0 optimized structures

Model compound	$E_{total}(S_0)$ (eV)	$E_{total}(S_1)$ (eV)	$E_{S0}(S_0 \rightarrow S_1)$ (eV)	Excited-state wavefunction (contribution ratio)
$[Ti(OH)_2(H_2O)_2$-(μ-O)$_2$-AA]	-50010.3381	-50008.9356	2.19	HOMO→LUMO (100%)
$[Ti(OH)_2(H_2O)_2$-(μ-O)$_2$-BZ]	-41789.7701	-41788.0711	2.41	HOMO→LUMO (99%)
$[Ti(OH)_3(H_2O)_2$-(μ-O)-TCNQ]$^-$	-53989.6840	-53987.6132	2.41	HOMO→LUMO (100%)
$[Ti(OH)_3(H_2O)$-(μ-OOC)-AT]	-51189.5128	-51186.8800	2.88	HOMO→LUMO (98%)

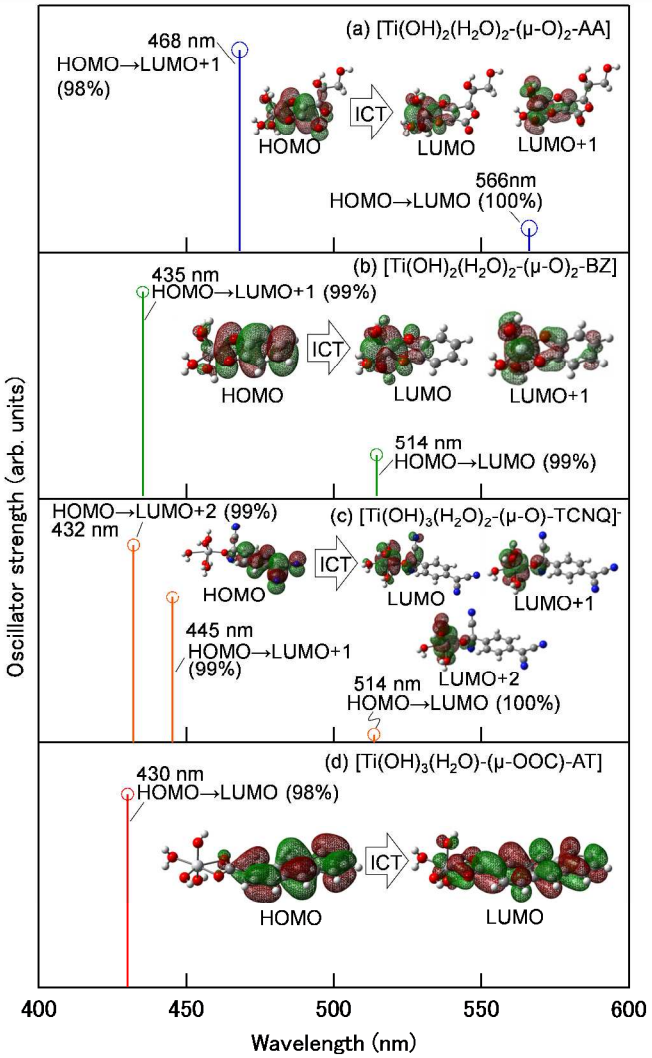

Fig. 5. Calculated electronic-excitation spectra in the S_0 optimized structures of (a) $[Ti(OH)_2(H_2O)_2$-(μ-O)$_2$-AA], (b) $[Ti(OH)_2(H_2O)_2$-(μ-O)$_2$-BZ], (c) $[Ti(OH)_3(H_2O)_2$-(μ-O)-TCNQ]$^-$, and (d) $[Ti(OH)_3(H_2O)$-(μ-OOC)-AT]. The electronic distributions (|isovalue|=0.02) of molecular orbitals in the S_0 optimized structures are shown. Green and brown isosurfaces stand for opposite signs in amplitude. The values in brackets denote the contribution ratios of one-electron excitation electronic configurations.

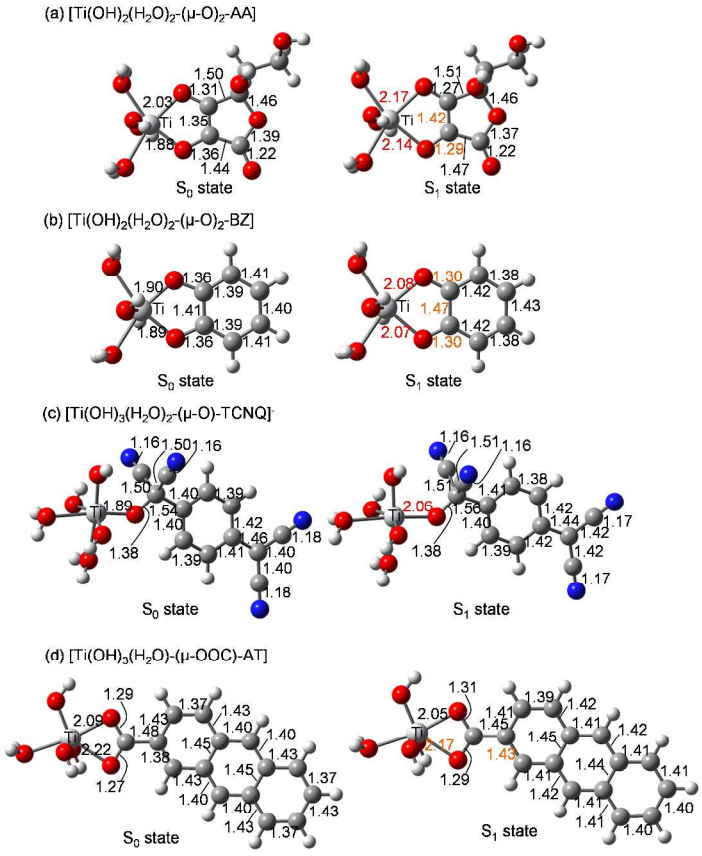

Fig. 6. Optimized structures in the S_0 and S_1 states of (a) $[Ti(OH)_2(H_2O)_2$-(μ-O)$_2$-AA], (b) $[Ti(OH)_2(H_2O)_2$-(μ-O)$_2$-BZ], (c) $[Ti(OH)_3(H_2O)_2$-(μ-O)-TCNQ]$^-$, and (d) $[Ti(OH)_3(H_2O)$-(μ-OOC)-AT]. Bond lengths are shown in a unit of Å. Bond-length changes larger 0.1 Å and in the range of 0.05-0.1 Å are shown in red and orange numbers, respectively. Gray: carbon, white: hydrogen, blue: nitrogen, red: oxygen, large white: titanium atom.

Structural changes in ICT excited states

Fig. 6 shows the optimized structures in the S_0 and S_1 states of the four model compounds. Large structural changes between the S_0 and S_1 states are seen on the adsorption moieties.

In $[Ti(OH)_2(H_2O)_2$-(μ-$O)_2$-AA], the Ti-O_{bridge} bond lengths significantly increase by 0.14 and 0.26 Å, the O_{bridge}-C bond lengths decreases by 0.04 and 0.07 Å, and the adjacent C=C bond length increases by 0.07 Å in the S_1 state, as shown by red and orange numbers in Fig. 6(a). Similarly, $[Ti(OH)_2(H_2O)_2$-(μ-$O)_2$-BZ] shows striking bond-length changes around the adsorption moiety in the S_1 state, as shown in Fig. 6(b). On the other hand, in $[Ti(OH)_3(H_2O)_2$-(μ-O)-TCNQ]$^-$ the Ti-O bond is just elongated by 0.17 Å in the S_1 state, as shown in Fig. 5(c). $[Ti(OH)_3(H_2O)$-(μ-OOC)-AT] shows no bond lengths changes larger than 0.05 Å, as shown in Fig. 6(d). From these results, it is considered that reorganization energies in $[Ti(OH)_2(H_2O)_2$-(μ-$O)_2$-AA] and $[Ti(OH)_2(H_2O)_2$-(μ-$O)_2$-BZ] are much larger than those in $[Ti(OH)_3(H_2O)_2$-(μ-O)-TCNQ]$^-$ and $[Ti(OH)_3(H_2O)$-(μ-OOC)-AT]. The calculated $E_{total}(S_1)$ values are tabulated in Table 1.

Table 2. Calculated reorganization energies (λ^{calc}), energy gaps (ΔE^{calc}), activation energies (E_a^{calc}) estimated from λ^{calc} and ΔE^{calc}, experimental energy gaps (ΔE^{exp}), and activation energies ($E_a^{calc+exp}$) estimated from λ^{calc} and ΔE^{exp} in $[Ti(OH)_2(H_2O)_2$-(μ-$O)_2$-AA], $[Ti(OH)_2(H_2O)_2$-(μ-$O)_2$-CA], $[Ti(OH)_3(H_2O)_2$-(μ-O)-TCNQ]$^-$, and $[Ti(OH)_3(H_2O)$-(μ-OOC)-AT].

Model compound	λ^{calc} (eV)	ΔE^{calc} (eV)	ΔE^{exp} (eV)	E_a^{calc} (eV)	$E_a^{calc+exp}$ (eV)
$[Ti(OH)_2(H_2O)_2$-(μ-$O)_2$-AA]	0.79	1.4	2.1	0.12	0.54
$[Ti(OH)_2(H_2O)_2$-(μ-$O)_2$-BZ]	0.71	1.7	2.3	0.35	0.89
$[Ti(OH)_3(H_2O)_2$-(μ-O)-TCNQ]$^-$	0.34	2.1	1.8	2.2	1.6
$[Ti(OH)_3(H_2O)$-(μ-OOC)-AT]	0.25	2.6	2.1	5.7	3.4

Reorganization and activation energies

Reorganization energies were estimated from Eq 3 with the calculated $E_{total}(S_0)$, $E_{total}(S_1)$, and $E_{S0}(S_0 \rightarrow S_1)$ in Table 1. As shown in Table 2, the reorganization energies in $[Ti(OH)_2(H_2O)_2$-(μ-$O)_2$-AA] and $[Ti(OH)_2(H_2O)_2$-(μ-$O)_2$-BZ] were estimated to be 0.79 and 0.71 eV, respectively. On the other hand, $[Ti(OH)_3(H_2O)_2$-(μ-O)-TCNQ]$^-$ and $[Ti(OH)_3(H_2O)$-(μ-OOC)-AT] show smaller reorganization energies of 0.34 and 0.25 eV, respectively. This result is consistent with the mentioned prediction from the structural changes in the S_1 states. Fig. 7(a) shows the relationship between the reported IPCE maximum values and the calculated reorganization energies. Interestingly, there is a certain correlation between the IPCE values and reorganization energies. The IPCE value gradually decreases in the range between 0.2 and 0.3 eV, and then drastically reduces in the range between 0.3 and 0.6 eV, and then saturates in the range between 0.6 and 0.8 eV, as shown by a dashed curve in Fig. 7(a). This behavior evidently indicates that the reorganization energy is a key factor to determine the IPCE values.

From the above DFT and TD-DFT calculations, the energy gap (ΔE^{calc}) was estimated as 1.4 eV for $[Ti(OH)_2(H_2O)_2$-(μ-$O)_2$-AA], 1.7 eV for $[Ti(OH)_2(H_2O)_2$-(μ-$O)_2$-BZ], 2.1 eV for $[Ti(OH)_3(H_2O)_2$-(μ-O)-TCNQ]$^-$, and 2.6 eV for $[Ti(OH)_3(H_2O)$-(μ-OOC)-AT], as shown in Table 2. The ΔE^{calc} values are comparable to the experimental onset energies (ΔE^{exp}) of the ICT absorption bands and IPCE spectra except for $[Ti(OH)_2(H_2O)_2$-(μ-$O)_2$-AA]. The ΔE^{calc} (1.4 eV) for $[Ti(OH)_2(H_2O)_2$-(μ-$O)_2$-AA] is much smaller than the reported IPCE onset energy (ca. 2.1 eV). [7,8] With the calculated reorganization energies and energy gaps, the activation energies (E_a^{calc}) for $[Ti(OH)_2(H_2O)_2$-(μ-$O)_2$-AA], $[Ti(OH)_2(H_2O)_2$-(μ-$O)_2$-BZ], $[Ti(OH)_3(H_2O)_2$-(μ-O)-TCNQ]$^-$, and $[Ti(OH)_3(H_2O)$-(μ-OOC)-AT] were estimated by Eq 2 to be 0.12, 0.35, 2.2, 5.7 eV, respectively (Table 2). Note that the estimated activation

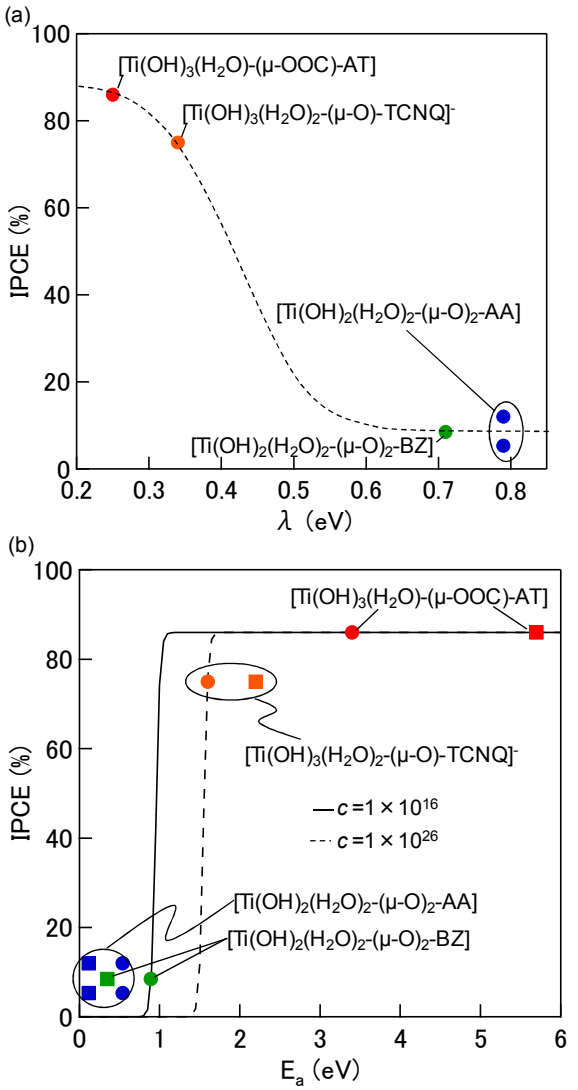

Fig. 7. Relationships of the reported IPCE maxima with (a) calculated reorganization energies and (b) calculated activation energies (squares: E_a^{calc}, circles: $E_a^{calc+exp}$) for $[Ti(OH)_2(H_2O)_2$-(μ-$O)_2$-AA] (blue), $[Ti(OH)_2(H_2O)_2$-(μ-$O)_2$-BZ] (green), $[Ti(OH)_3(H_2O)_2$-(μ-O)-TCNQ]$^-$ (orange) and $[Ti(OH)_3(H_2O)$-(μ-OOC)-AT] (red). Dashed curve in (a) stands for a qualitative behaviour. Solid and dashed curves in (b) denote the dependences of the IPCE on the activation energy for carrier recombination based on the Marcus theory (Eq 6) with *LHE* of 0.86, assuming that the *c* factor is a constant (1×10^{16} and 1×10^{26}, respectively). See text for detail.

energies tend to be overestimated, since reorganization energies in TiO_2 nanoparticles are not taken into account. The estimated activation energies show a tendency that E_a^{calc} increases in the order of AA < CA < TCNQ < AT-COOH. Activation energies

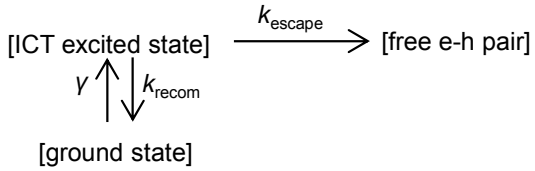

Fig. 8. Kinetic scheme of ICT excited state dynamics.

($E_a^{calc+exp}$) were also calculated with the calculated reorganization energies ((λ^{calc}) and experimental energy gaps (ΔE^{exp}) (Table 2). $E_a^{calc+exp}$ was estimated as 0.54, 0.89, 1.6, and 3.4 eV for $[Ti(OH)_2(H_2O)_2$-(μ-O)$_2$-AA], $[Ti(OH)_2(H_2O)_2$-(μ-O)$_2$-BZ], $[Ti(OH)_3(H_2O)_2$-(μ-O)-TCNQ]$^-$, and $[Ti(OH)_3(H_2O)$-(μ-OOC)-AT], respectively (Table 2). The estimated $E_a^{calc+exp}$ increases in the order of AA < CA < TCNQ < AT-COOH similarly to E_a^{calc}. Fig. 7(b) shows the relationship between the IPCE values and activation energies (squares: E_a^{calc}, circles: $E_a^{calc+exp}$). A clear correlation between the IPCE values and activation energies is found. $[Ti(OH)_3(H_2O)$-(μ-OOC)-AT] and $[Ti(OH)_3(H_2O)_2$-(μ-O)-TCNQ]$^-$ show the larger activation energies than 1.5 eV for the higher IPCE values and $[Ti(OH)_2(H_2O)_2$-(μ-O)$_2$-AA] and $[Ti(OH)_2(H_2O)_2$-(μ-O)$_2$-BZ] show the smaller activation energies than 1 eV for the low IPCE values. In addition, the IPCE rapidly increases around 1.25 eV.

Activation-energy dependence of IPCE

In order to analyse the activation-energy dependence, the IPCE is formulated with a simple kinetic scheme for the ICT excited state, as shown in Fig. 8. In the kinetic scheme, the ICT excited state is relaxed to the ground state by electron-hole recombination with a rate constant of k_{recom}. In competition with the carrier recombination, the ICT excited state changes to a free electron-hole pair with a rate constant of k_{escape} by penetration of photoinjected electrons inside of TiO_2 nanoparticles. Since free electron-hole pairs are detected as photocurrent, an absorbed photon-to-current conversion efficiency (*APCE*) is expressed by the following equation.

$$APCE(\%) = \frac{100 \times k_{escape}}{k_{escape} + k_{recom}} \quad (4)$$

Since IPCE is a product of a light-harvesting quantum efficiency (LHE) and APCE, IPCE is described as follows.

$$IPCE(\%) = \frac{100 \times LHE}{1 + (k_{recom}/k_{escape})} \quad (5)$$

Substituting Eq 1 in Eq 5, the IPCE is formulated by the following equation.

$$IPCE(\%) = \frac{100 \times LHE}{1 + c \times exp\left(-\frac{E_a}{k_B T}\right)} \quad (6)$$

$$c = \frac{2\pi^2}{k_{escape} h} \frac{\beta^2}{\sqrt{\pi \lambda k_B T}} \quad (7)$$

The IPCE is a function of three variables of LHE, c, and E_a. LHE generally depends on ICT absorption coefficient in photovoltaic cells and optical path length enhanced by

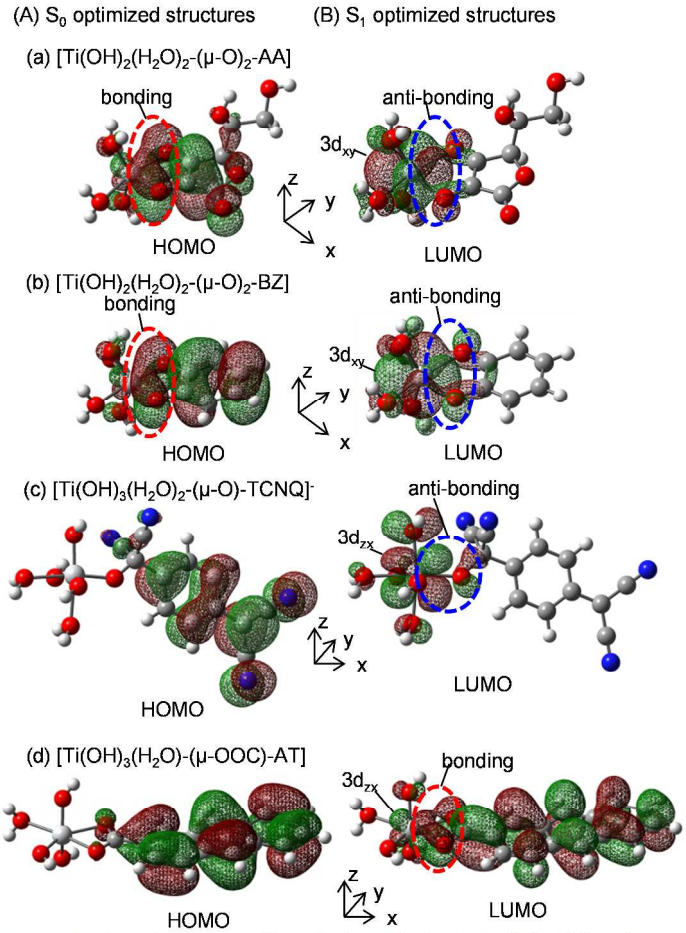

Fig. 9. Electronic distributions (|isovalue|=0.02) of HOMOs (*left side*) in the S_0 optimized structures and LUMOs (right side) in the S_1 optimized structures of (a) $[Ti(OH)_2(H_2O)_2$-(μ-O)$_2$-AA], (b) $[Ti(OH)_2(H_2O)_2$-(μ-O)$_2$-BZ], (c) $[Ti(OH)_3(H_2O)_2$-(μ-O)-TCNQ]$^-$, and (d) $[Ti(OH)_3(H_2O)$-(μ-OOC)-AT]. Gray: carbon, white: hydrogen, blue: nitrogen, red: oxygen, large white: titanium atom. Green and brown isosurfaces stand for opposite signs in amplitude.

scattering effects. The reported data indicate that LHE values at the IPCE-maximum wavelengths are close to 1.[2,9,10] Fig. 7(b) shows the calculated curves obtained by Eq 6 with LHE of 0.86 and c of 1×10^{16} (solid curve) and 1×10^{26} (dashed curve)). It is noteworthy that the theoretical curves well reproduce the activation-energy dependence of the IPCE, which indicates that all the IPCE data in Fig. 2 is successfully explained by the Marcus theory. The other important point is that even with the much different c values the calculated IPCE curve hardly changes. This result indicates that the carrier recombination is not governed by c, but by the activation energy. Since the estimated activation energies predominantly depend on the reorganization energies, the carrier recombination can be suppressed by control of the reorganization energy.

Origin of reorganization energy

As mentioned above, the calculated reorganization energies are predominantly attributed to the bond-length changes on the chemical adsorption moieties. In the Marcus theory, the reorganization energy is given by the following equation.

$$\lambda = \frac{k}{2}\Delta {q_{S_1}}^2 \qquad (8)$$

The chemical-adsorption strength (k) is qualitatively evaluated from the Ti-O_{bridge} bond strength and the number of Ti-O_{bridge} bonds. Table 4 shows the bond strengths qualitatively evaluated from the Ti-O_{bridge} bond lengths in Fig. 6 and the number of Ti-O_{bridge} bonds in the model compounds. From this table, it is seen that the diol chemisorption in [$Ti(OH)_2(H_2O)_2$-(μ-O)$_2$-AA] and [$Ti(OH)_2(H_2O)_2$-(μ-O)$_2$-BZ] shows the stronger and more Ti-O_{bridge} bonds as compared to the other compounds. Therefore, the k value for these model compounds is considered to be larger than those in the other ones. In addition, the diol chemisorption shows the larger Ti-O_{bridge} bond-length changes (Δq_{S1}) as compared to the other compounds. (Fig. 6) These two factors explain the larger reorganization energies for the diol chemisorption. Since the reorganization energy increases with the square of Δq_{S1}, the Ti-O_{bridge} bond-length changes are considered to predominantly contribute the larger reorganization energies.

The Ti-O_{bridge} bond-length changes result from the change of molecular-orbital interaction on the chemisorption site in the S_1 state. Fig. 9 shows the electronic distributions of HOMOs in the S_0 optimized structures and LUMOs in the S_1 optimized structures of the model compounds. It was confirmed that the electronic distributions of the HOMOs in the S_1 optimized structures are almost the same as those in the S_0 optimized ones. In the [$Ti(OH)_2(H_2O)_2$-(μ-O)$_2$-AA] and [$Ti(OH)_2(H_2O)_2$-(μ-O)$_2$-BZ], the molecular-orbital interactions on the Ti-O_{bridge} bonds are bonding for the HOMOs and anti-bonding for the LUMOs, respectively, as shown by red and blue dashed ellipses in Figs. 9(a) and 9(b). On the other hand, in [$Ti(OH)_3(H_2O)_2$-(μ-O)-TCNQ]$^-$, the HOMO has no distribution on the Ti-O_{bridge} bond and the LUMO has an anti-bonding interaction, as shown in Fig. 9(c). In [$Ti(OH)_3(H_2O)$-(μ-OOC)-AT], the HOMO has no distribution on the Ti-O_{bridge} band and the LUMO has a bonding interaction, as shown in Fig. 9(d). These results are summarized in Table 4. In the case of the diol chemisorption, the molecular-orbital interaction on the Ti-O_{bridge} bonds drastically changes from bonding to antibonding. This drastic change induces the large bond-length changes, giving rise to the larger reorganization energies.

Table 3. Qualitative bond strengths and numbers of Ti-O_{bridge} bonds, molecular-orbital interactions on the Ti-O_{bridge} bonds in HOMOs in the S_0 optimized structures and LUMOs in the S_1 optimized structures, and qualitative magnitudes of reorganization energies in [$Ti(OH)_2(H_2O)_2$-(μ-O)$_2$-AA], [$Ti(OH)_2(H_2O)_2$-(μ-O)$_2$-CA], [$Ti(OH)_3(H_2O)_2$-(μ-O)-TCNQ]$^-$, and [$Ti(OH)_3(H_2O)$-(μ-OOC)-AT].

Model compound	Ti-O_{bridge}	Number of Ti-O_{bridge}	Ti-O_{bridge} molecular-orbital interaction		Reorganization energy
			HOMO in S_0 optimized structure	LUMO in S_1 optimized structure	
[$Ti(OH)_2(H_2O)_2$-(μ-O)$_2$-AA]	strong	2	bonding	anti-bonding	large
[$Ti(OH)_2(H_2O)_2$-(μ-O)$_2$-BZ]	strong	2	bonding	anti-bonding	large
[$Ti(OH)_3(H_2O)_2$-(μ-O)-TCNQ]$^-$	strong	1	none	anti-bonding	small
[$Ti(OH)_3(H_2O)$-(μ-OOC)-AT]	weak	2	none	bonding	small

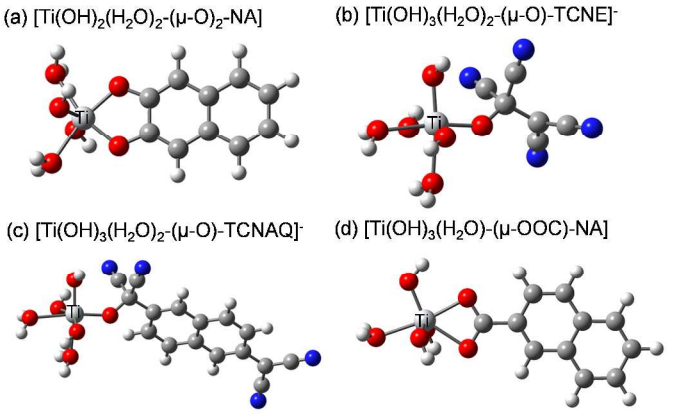

Fig. 10. Calculated S_0 optimzied structures of (a) [$Ti(OH)_2(H_2O)_2$-(μ-O)$_2$-NA], (b) [$Ti(OH)_3(H_2O)_2$-(μ-O)-TCNE]$^-$, (c) [$Ti(OH)_3(H_2O)_2$-(μ-O)-TCNAQ]$^-$, and (d) [$Ti(OH)_3(H_2O)$-(μ-OOC)-NA]. Gray: carbon, white: hydrogen, blue: nitrogen, red: oxygen, large white: titanium atom.

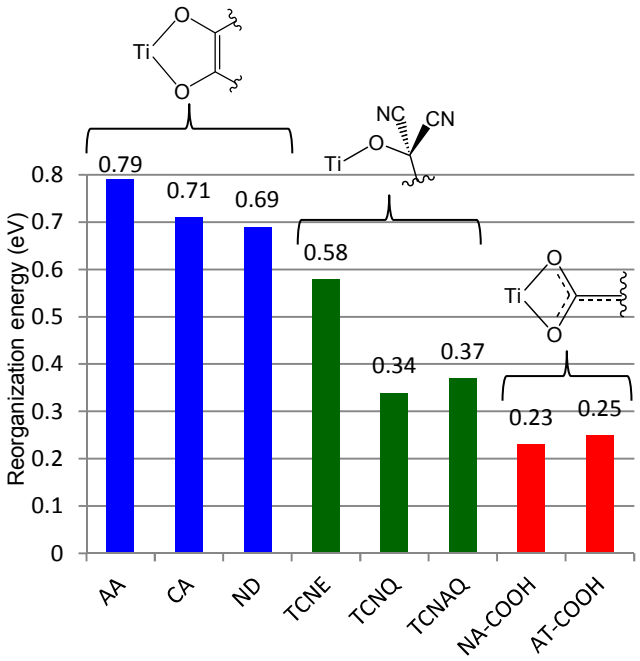

Fig. 11. Calculated reorganization energies in [$Ti(OH)_2(H_2O)_2$-(μ-O)$_2$-AA], [$Ti(OH)_2(H_2O)_2$-(μ-O)$_2$-BZ], [$Ti(OH)_2(H_2O)_2$-(μ-O)$_2$-NA], [$Ti(OH)_3(H_2O)_2$-(μ-O)-TCNE]$^-$, [$Ti(OH)_3(H_2O)_2$-(μ-O)-TCNQ]$^-$, [$Ti(OH)_3(H_2O)_2$-(μ-O)-TCNAQ]$^-$, [$Ti(OH)_3(H_2O)$-(μ-OOC)-NA], and [$Ti(OH)_3(H_2O)$-(μ-OOC)-AT].

Organic-moiety dependence

Table 4. Calculated reorganization energies (λ^{calc}), energy gaps (ΔE^{calc}), activation energies (E_a^{calc}) estimated from λ^{calc} and ΔE^{calc}, experimental energy gaps (ΔE^{exp}), and activation energies ($E_a^{calc+exp}$) estimated from λ^{calc} and ΔE^{exp} in $[Ti(OH)_2(H_2O)_2$-(μ-O)$_2$-NA], $[Ti(OH)_3(H_2O)_2$-(μ-O)-TCNE]$^-$, $[Ti(OH)_3(H_2O)_2$-(μ-O)-TCNAQ]$^-$, and $[Ti(OH)_3(H_2O)$-(μ-OOC)-NA]. The reported IPCE maximum values for the ICT transitions in TiO_2-TCNE and TiO_2-TCNAQ are shown.

Model compound	λ^{calc} (eV)	ΔE^{calc} (eV)	ΔE^{exp} (eV)	E_a^{calc} (eV)	$E_a^{calc+exp}$ (eV)	$IPCE_{Max}$
$[Ti(OH)_2(H_2O)_2$-(μ-O)$_2$-NA]	0.69	1.9	–	0.53	–	–
$[Ti(OH)_3(H_2O)_2$-(μ-O)-TCNE]$^-$	0.58	2.4	2.1	1.4	1.0	36%@490 nm
$[Ti(OH)_3(H_2O)_2$-(μ-O)-TCNAQ]$^-$	0.37	2.0	1.6	1.8	1.0	57%@480 nm
$[Ti(OH)_3(H_2O)$-(μ-OOC)-NA]	0.23	3.4	–	11	–	–

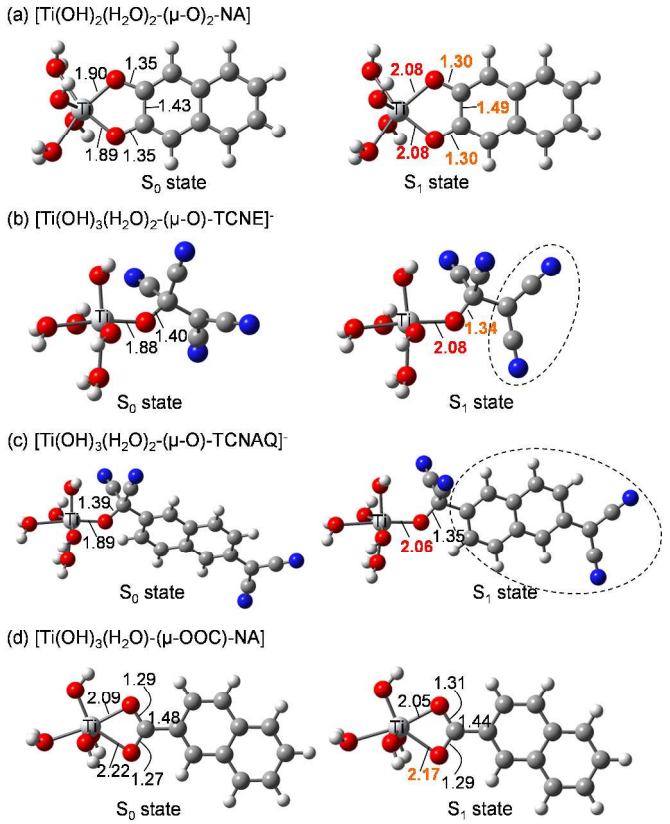

Fig. 12. Optimized structures and bond lengths around the coordination sites in the S_0 and S_1 states of (a) $[Ti(OH)_2(H_2O)_2$-(μ-O)$_2$-NA], (b) $[Ti(OH)_3(H_2O)_2$-(μ-O)-TCNE]$^-$, (c) $[Ti(OH)_3(H_2O)_2$-(μ-O)-TCNAQ]$^-$, and (d) $[Ti(OH)_3(H_2O)$-(μ-OOC)-NA]. Bond lengths are shown in a unit of Å. Bond-length changes larger 0.1 Å and in the range of 0.05-0.1 Å are shown in red and orange, respectively. Gray: carbon, white: hydrogen, blue: nitrogen, red: oxygen, large white: titanium atom.

In order to confirm the important role of the chemical adsorption, additional four model compounds with different aromatic moieties, $[Ti(OH)_2(H_2O)_2$-(μ-O)$_2$-NA] (NA: naphthalene), $[Ti(OH)_3(H_2O)_2$-(μ-O)-TCNE]$^-$ (TCNE: tetracyanoethylene), $[Ti(OH)_3(H_2O)_2$-(μ-O)-TCNAQ]$^-$ (TCNAQ: 11,11,12,12-tetracyanonaphthoquinodimethane), and $[Ti(OH)_3(H_2O)$-(μ-OOC)-NA] (Fig. 10) were examined. At first, TD-DFT calculations indicated that all these model compounds show ICT transitions, similarly to the mentioned model compounds. Reorganization energies for those model compounds were estimated from the calculated $E_{total}(S_0)$, $E_{total}(S_1)$ and $E_{S0}(S_0 \rightarrow S_1)$ in the same manner as the above, as shown in Table 4. The reorganization energies in $[Ti(OH)_3(H_2O)_2$-(μ-O)-TCNAQ]$^-$, and $[Ti(OH)_3(H_2O)$-(μ-

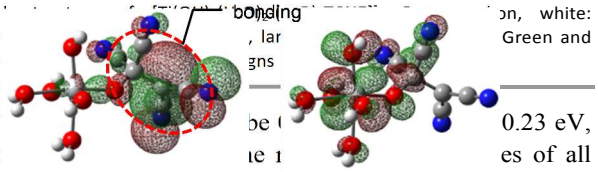

Fig. 13. Electronic distributions (|isovalue|=0.02) of HOMO and LUMO in the S_0 optimize … on, white: hydroge… , lar… Green and brown is… gns

OOC)- … be … 0.23 eV, respect… ıe … es of all the model complexes studied in this work. Interestingly, it is found that the reorganization energy does not remarkably depend on the kind of organic moiety, but the kind of chemical adsorption except for TCNE. The diol chemisorption shows the larger reorganization energies of 0.69–0.79 eV. The nucleophilic-addition chemisorption for TCNQ and TCNAQ shows the moderate reorganization energies of 0.34 and 0.37 eV. In contrast, the reorganization energy for TCNE was estimated as 0.58 eV remarkably larger than those for TCNQ and TCNAQ. On the other hand, the carboxylate chemisorption exhibits smaller reorganizations of 0.23 and 0.25 eV. From this result, it is indicated that the selection of chemical anchor is essential to suppress carrier recombination. It is noteworthy that the carboxylate chemical adsorption that has been extensively utilized for dye-sensitized solar cells [28,29] shows such small reorganization energies beneficial to suppress carrier recombination.

Fig. 12 shows the optimized structures in the S_0 and S_1 states of the added four model compounds. As shown in Fig. 12(a), $[Ti(OH)_2(H_2O)_2$-(μ-O)$_2$-NA] shows larger bond-length changes on the adsorption moiety consistent with the larger reorganization energy, similarly to $[Ti(OH)_2(H_2O)_2$-(μ-O)$_2$-AA] and $[Ti(OH)_2(H_2O)_2$-(μ-O)$_2$-BZ]. $[Ti(OH)_3(H_2O)$-(μ-OOC)-NA] show similar bond-length changes to $[Ti(OH)_3(H_2O)$-(μ-OOC)-AT], as shown in Fig. 12(d). On the other hand, in $[Ti(OH)_3(H_2O)_2$-(μ-O)-TCNE]$^-$ and $[Ti(OH)_3(H_2O)_2$-(μ-O)-TCNAQ]$^-$ another structural change occurs as compared with $[Ti(OH)_3(H_2O)_2$-(μ-O)-TCNQ]$^-$. As shown in Figs. 12(b) and 12(c), the dicyanomethylene group far from the coordination site tilts in the S_1 state. Especially, in $[Ti(OH)_3(H_2O)_2$-(μ-O)-TCNE]$^-$, the dicyanomethylene group tilts almost vertically.

Since the HOMO in the S_0 optimal state has quite large electronic distribution with the π-bonding property on the

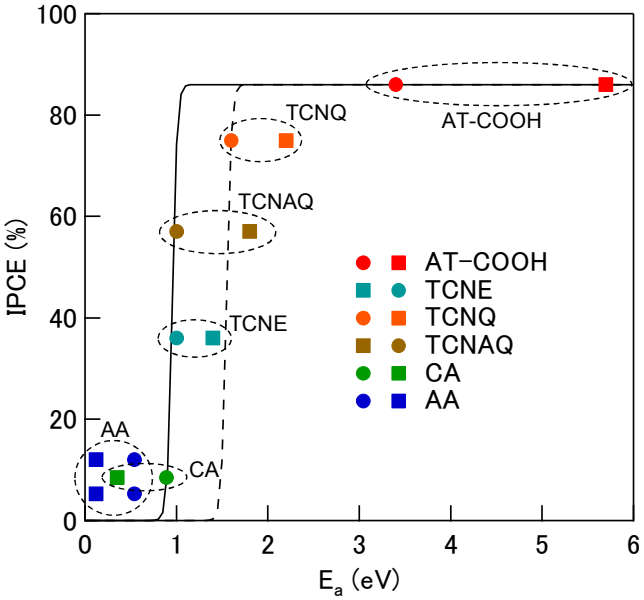

Fig. 14. Relationship between the reported IPCE maxima and calculated reorganization energies (squares: E_a^{calc}, circles: $E_a^{calc+exp}$) for $[Ti(OH)_2(H_2O)_2\text{-}(\mu\text{-}O)_2\text{-}AA]$ (blue), $[Ti(OH)_2(H_2O)_2\text{-}(\mu\text{-}O)_2\text{-}BZ]$ (green), $[Ti(OH)_3(H_2O)_2\text{-}(\mu\text{-}O)\text{-}TCNE]^-$ (water blue), $[Ti(OH)_3(H_2O)_2\text{-}(\mu\text{-}O)\text{-}TCNQ]^-$ (orange), $[Ti(OH)_3(H_2O)_2\text{-}(\mu\text{-}O)\text{-}TCNAQ]^-$ (dark yellow), and $[Ti(OH)_3(H_2O)\text{-}(\mu\text{-}OOC)\text{-}AT]$ (red). Solid and dashed curves denote the theoretical curves of the IPCE (Eq 6) with *LHE* of 0.86 and *c* of 1×10^{16} and 1×10^{26}, respectively.

ethylene bond, as shown in Fig. 13, the ICT transition significantly weakens the C=C π-bonding property and then results in the rotation of the dicyanomethylene group. This structural change increases the reorganization energy in $[Ti(OH)_3(H_2O)_2\text{-}(\mu\text{-}O)\text{-}TCNE]^-$.

The IPCE maximum values of the TiO_2-TCNE and TiO_2-TCNAQ based photovoltaic cells were reported to 36% at 490 nm and 57% at 480 nm, respectively.[9] The IPCE data were plotted as a function of the calculated activation energy ((squares: E_a^{calc}, circles: $E_a^{calc+exp}$)), as shown in Figure 14. The IPCE data of TCNE and TCNAQ are in good agreement with the two theoretical curves. Together with the above mentioned data, all the reported IPCE data were well reproduced by Eq 6. The reduction in the IPCE in TCNE is attributed to the decreased activation energy owing to the larger reorganization energy. On the other hand, the reorganization energy for TCNAQ is almost the same as that for TCNQ. The lowering of the IPCE results from the decrease of the activation energy due to the reduction of the energy gap that corresponds to the red-shift of the ICT absorption onset [9,14].

A guiding principle for efficient photovoltaic conversion

The suppression of carrier recombination have been the significant problem for ICT transitions, as described in the introduction. It has been considered that electronic coupling at organic-inorganic interfaces not only allows for ICT transitions, but also opens up a channel for carrier recombination. However, this work revealed that the contribution of the interfacial electronic coupling to carrier recombination is rather small and

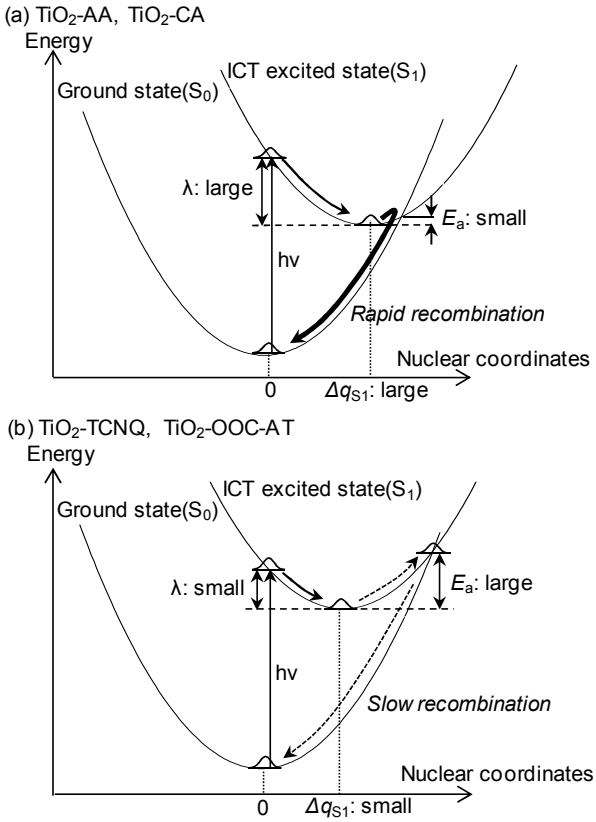

Fig. 15. Potential curves of the S_0 and ICT S_1 states for $[Ti(OH)_2(H_2O)_2\text{-}(\mu\text{-}O)_2\text{-}AA]$, $[Ti(OH)_2(H_2O)_2\text{-}(\mu\text{-}O)_2\text{-}BZ]$, $[Ti(OH)_3(H_2O)_2\text{-}(\mu\text{-}O)\text{-}TCNQ]^-$, and $[Ti(OH)_3(H_2O)\text{-}(\mu\text{-}OOC)\text{-}AT]$.

the reorganization energy governs the carrier-recombination rate. The rapid carrier recombination in TiO_2-CA [8] is not attributed to the large electronic coupling, but to the large reorganization energy, as shown in Fig. 15(a). On the other hand, TiO_2-TCNQ and TiO_2-OOC-AT show the smaller reorganization energies, suppressing the carrier recombination for the efficient light-to-current conversions, as shown in Fig 15(b). Therefore, in order to accomplish efficient photovoltaic conversions due to ICT transitions, larger interfacial electronic coupling and smaller reorganization energy are required.

Conclusion

In this work, the photovoltaic conversion due to the ICT transitions and carrier recombination were studied based on the Marcus theory with DFT and TD-DFT calculations. All the so-far reported IPCE values for the organic-to-inorganic ICT transitions were successfully explained in terms of the reorganization and activation energies. This result reveals that carrier recombination can be suppressed by the reduction of the reorganization energy, leading to the enhancement of the IPCE.

This knowledge is crucial for efficient photovoltaic conversion by ICT transitions.

Acknowledgements

This research was supported by the Precursory Research for Embryonic Science and Technology (PRESTO) program of the Japan Science and Technology Agency (JST).

Notes and references

[a]Research Center for Advanced Science and Technology (RCAST), The University of Tokyo, 4-6-1 Komaba, Meguro-ku, Tokyo 153-8904, Japan. Present affiliation: Graduate School of Science and Technology, Gunma University, 1-5-1 Tenjin-cho, Kiryu, Gunma, 376-8515, Japan. E-mail: jfujisawa@gunma-u.ac.jp
[b]Japan Science and Technology Agency (JST), Precursory Research for Embryonic Science and Technology (PRESTO), 4-1-8 Honcho Kawaguchi, Saitama 332-0012, Japan.

1 A. P. Xagas, M. C. Bernard, A. Hugot-Le Goff, N. Spyrellis, Z. Loizos and P. Falaras, *J. Photochem. Photobiol. A: Chem.*, 2000, **132**, 115.
2 M. Sirimanne and T. Soga, *Sol. Energ. Mat. Sol. C*., 2003, **80**, 383.
3 E. L. Tae, S. H. Lee, J. K. Lee, S. S. Yoo, E. J. Kang and K. B. Yoon, *J. Phys. Chem. B*, 2005, **109**, 22513.
4 J. Fujisawa and T. Ishihara, *Phys. Rev. B*, 2004, **70**, 113203.
5 J. Fujisawa and N. Tajima, *Phys. Rev. B*, 2005, **72**, 125201.
6 J. Fujisawa, N. Tajima, K. Tamaki, M. Shimomura and T. Ishihara, *J. Phys. Chem. C*, 2007, **111**, 1146.
7 J. Fujisawa and G. Giacomo, *Phys. Chem. Phys. Chem.*, 2014, **16**, 17955.
8 Y. Wang, K. Hang, N. A. Anderson and T. Lian, *J. Phys. Chem. B*, 2003, **107**, 9434.
9 T. Kubo, J. Fujisawa and H. Segawa, *Electrochemistry*, 2009, **77**, 977.
10 J. Fujisawa and M. Nagata, *Chem. Phys. Lett*., 2015, **619**, 180.
11 R. A. Marcus, *Rev. Mod. Phys*., 1993, **65**, 599.
12 V. Balzani, A. Juris, M. Venturi, S. Campagna and S. Serroni, *Chem. Rev*., 1996, **96**, 759.
13 R. Jono, J. Fujisawa, H. Segawa and K. Yamashita, *J. Phys. Chem. Letters*, 2011, 2, 1167.
14 S. Manzhos, R. Jono, K. Yamashita, J. Fujisawa, M. Nagata and H. Segawa, *J. Phys. Chem. C*, 2011, **115**, 21487.
15 R. Jono, J. Fujisawa, H. Segawa and K. Yamashita, *Phys. Chem. Chem. Phys*. 2013, **15**, 18584.
16 Kohn W and Sham, *Phys. Rev*., 1965, **140**, A1133.
17 A.D. Becke, *J. Chem. Phys.*, 1993, **98**, 5648.
18 C. Lee, W. Yang and R. G. Parr, *Phys. Rev. B*, 1988, **37**, 785.
19 R. Ditchfield, W. Hehre and J. Pople, *J. Chem. Phys.*, 1971, **54**, 724.
20 W. Hehre, R. Ditchfield and J. Pople, *J. Chem. Phys.*, 1972, **56**, 2257.
21 M. A. L. Marques and E. K. U. Gross. *Annu. Rev. Phys. Chem.* 2004, **55**, 427.
22 V. Barone and M. Cossi, *J. Phys. Chem. A*, 1998, **102**, 1995.
23 M. Cossi, N. Rega, G. Scalmani and V. Barone, *J. Comput. Chem*., 2003, **24**, 669.
24 Y. Takano and K. N. Houk, *J. Chem. Theory Comput.*, 2005, **1**, 70.
25 M. J. Frisch *et al*. Gaussian 09, revision D.01; Gaussian, Inc.: Wallingford, CT, 2009.
26 T. Yanai, D. P Tew and N. C Handy, *Chem. Phys. Lett*., 2004, **393**, 51.
27 M. J. G. Peach, P. Benfield, T. Helgaker and D. J. Tozer, *J. Chem. Phys.*, 2008, **128**, 044118.
28 K. Kalyanasundaram, *Dye-Sensitized Solar Cells*, EPFL Press, 2010.
29 T. Horiuchi, J. Fujisawa, S. Uchida and M. Grätzel, *Data Book on Dye-Sensitized Solar Cells*, CMC Publishing Co., Tokyo, 2009.

